Journal of
Marine Science and Engineering

MDPI

Article

Parametric Design of a New Float-Type Wave Energy Generator and Numerical Simulation of Its Hydrodynamic Performance

Yu Zhang * and Dongqin Li *

School of Naval Architecture and Ocean Engineering, Jiangsu University of Science and Technology, Zhenjiang 212100, China
* Correspondence: zhangyu_1003@163.com (Y.Z.); mandy_ldq@163.com (D.L.)

Abstract: A novel float-type device for wave energy power generation, designed specifically for offshore wave environments, is introduced as an innovative technology in wave energy utilization. Herein, we present the design concept, structural composition, and energy conversion process of the device, and conduct mathematical modeling and theoretical research on its kinematic and dynamic characteristics. At the same time, we use a numerical wave pool based on the STAR-CCM+ boundary wave making method and damping dissipation method to analyze the motion response and output power of the wave energy generator in a five-order Stokes wave environment within one wave cycle and the entire operating cycle. Finally, in order to develop the best design strategy, we study the effect of changing the structural parameters of the power generation device on the hydrodynamic performance of the device.

Keywords: wave power generation; oscillating float; computational fluid dynamics; hydrodynamic performance

Citation: Zhang, Y.; Li, D. Parametric Design of a New Float-Type Wave Energy Generator and Numerical Simulation of Its Hydrodynamic Performance. *J. Mar. Sci. Eng.* **2023**, *11*, 2192. https://doi.org/10.3390/jmse11112192

Academic Editors: Dong-Sheng Jeng, Abdellatif Ouahsine and Peng Du

Received: 11 October 2023
Revised: 9 November 2023
Accepted: 14 November 2023
Published: 17 November 2023

1. Introduction

The growth of the global economy and the excessive usage of fossil fuels have severely harmed and contaminated our ecosystem. Traditional energy sources are also becoming harder to obtain at the same time. As a result of this tendency, people are looking into new clean energy solutions to displace fossil fuels and numerous nations are gradually turning their focus to the large sector of ocean energy. Since waves have a tremendous amount of energy compared with wind and solar energy, developing and using wave energy offers several benefits, making coastal nations the center of interest for this technology today [1–3].

The design and analysis of hydrodynamic performance for wave energy power production devices represent a crucial field of study within marine renewable energy. Various types of power generation devices have been developed in this process. Due to its adaptable placement in the marine environment, oscillating float-type wave power generators [4] are one of the hotspots in the field of wave energy utilization and have high power generation efficiency.

Stephen Salter [5] created Salter's duck as a wave energy device. During the energy crisis, he was the first person to use the idea of oscillating floats to harness wave energy. This iconic tool is a springboard for further research on wave energy fields. In 2003, Korde [6] used a linked wave energy generation system with regular waves to numerically calculate the system's capture width ratio. In 2005, Eriksson et al. [7] performed some comparisons of the motion problem of a cylindrical float-type wave energy generator in regular and irregular waves, and they replaced the Power Take Off (PTO) mechanism in a wave energy power generator with linear springs and linear dampers. Babarit et al. [8] addressed the issue of energy capture efficiency in 2006 and offered two control approaches for the PTO system. The proposed method can adjust the device's energy capture efficiency in real time. In 2010, Griet et al. [9] used the Computational Fluid Dynamics (CFD) approach to simulate the absorbed power, impact velocity, and corresponding forces of the float under

varied slamming loads. They discovered that, although it is also related to power loss, the risk of the float destabilizing is highly dependent on the draught depth of the float and the ocean environment. However, the likelihood of the risk occurring can be significantly decreased by adjusting the relevant control parameters of the device. The hydrodynamic performance of a pendulous float in shallow nearshore water compared with a float in an offshore surge was examined by Negri et al. in 2018 [10]. They discovered that the efficiency of a wave energy system's power generation dramatically rises with increasing sea depth. Eliseo Marchesi [11] devised a plan for a two–float PTO system in 2020, and while PTO damping in irregular waves was evaluated, the numerical simulation findings and testing results were in accord. The same year, Christophe Vogel [12] researched the effects of wave attenuation on the hydrodynamic performance of an asymmetric float wave energy generator and a hybrid energy collection system.

It is crucial to acknowledge that the energy industry is highly intricate and encompasses the administration of various interrelated elements. As an illustration, apart from the aim of generating energy, it is essential to account for the endurance of the machinery, which needs to withstand the challenging oceanic setting. While studies have advanced and yielded outcomes, it remains conceivable to aspire for greater achievements [13]. To meet our energy requirements and diminish our reliance on non-renewable resources, our community is increasingly integrating more eco-friendly energy approaches. The utilization of the abundant ocean energy requires the creation of innovative technologies that will lower global CO_2 emissions from the burning of fossil fuels and turn ocean waves and tidal energy into a sustainable and economical energy source [14].

Numerical studies, simulation analyses, and experimental testing are common analytical approaches for oscillating float-type wave energy devices. Many scholars have conducted research in this field with the goal of improving the stability and reliability of the devices for power generation [15]. Based on the existing oscillating float wave power generation device, this paper intends to further simplify the structure and energy conversion process, with the design of a new wave power generation device. We use theoretical analysis and numerical simulation to study the hydrodynamic performance of the device and the captured energy characteristics. The final analysis conclusion drawn from the above aims to provide a certain technical basis and reference for future research.

2. Mechanical Theory

Accurately and scientifically predicting the energy conversion performance of power generation equipment is paramount in the realm of wave energy generation technology utilization. The mechanical behavior of these devices in the ocean is closely related to the efficiency of their energy conversion and structural reliability. As a result, the development and application of mechanical formulas will provide a critical theoretical foundation for the design of diverse wave energy devices.

2.1. Basic Control Equations

Fluid motion should adhere to the physical laws, such as the law of mass conservation, the law of momentum conservation, and the law of energy conservation. The law of conservation of energy is not taken into account when analyzing the hydrodynamic performance of a new oscillating float wave energy generator in an incompressible viscous fluid, and only the conservation law is expressed by using the equations for mass and momentum conservation [16].

Equation (1) is used in both steady flow and unsteady flow for incompressible fluids:

$$\frac{\partial u}{\partial x} + \frac{\partial v}{\partial y} = 0. \quad (1)$$

The Navier–Stokes equations for incompressible fluids can be reduced using the continuity Equation (2):

$$\begin{aligned}&\frac{\partial(\rho\cdot u)}{\partial t}+\frac{\partial\left(\rho\cdot u^2\right)}{\partial x}+\frac{\partial(\rho\cdot u\cdot v)}{\partial y}+\frac{\partial(\rho\cdot u\cdot w)}{\partial z}\\&=F_x-\frac{\partial p}{\partial x}+\frac{\partial}{\partial x}\left(2\mu\frac{\partial u}{\partial x}\right)+\frac{\partial}{\partial y}\left[\mu\left(\frac{\partial v}{\partial x}+\frac{\partial u}{\partial y}\right)\right]+\frac{\partial}{\partial z}\left[\mu\left(\frac{\partial u}{\partial z}+\frac{\partial w}{\partial x}\right)\right].\end{aligned} \tag{2}$$

The following condensed version is produced when the coefficient of viscosity is assumed to be uniform:

$$\rho\left[\frac{\partial u}{\partial t}+u\frac{\partial u}{\partial x}+v\frac{\partial u}{\partial y}+w\frac{\partial u}{\partial z}\right]=F_x-\frac{\partial p}{\partial x}+\mu\left[\frac{\partial^2 u}{\partial x^2}+\frac{\partial^2 u}{\partial y^2}+\frac{\partial^2 u}{\partial z^2}\right]. \tag{3}$$

2.2. Turbulence Model

In nature, turbulence dominates most flows, its flow field is extremely stochastic and pulsing, and its instantaneous flow satisfies the N–S equation. The *k*–equation model, the most widely employed two-equation model up to this point, was proposed by Launder and Spalding in 1974. The turbulence model is characterized by the following characteristic scales, which are based on Taylor's hypotheses regarding the length of the turbulence:

$$l_T\sim k^{3/2}/\varepsilon. \tag{4}$$

In the equation, k is the kinetic energy of turbulence, and ε is the dissipation rate of kinetic energy.

Similar to this, turbulent kinetic energy controls the typical velocity. As a result, the fundamental premise of the two-equation model is established, namely that the vortex viscosity coefficient can be written as follows:

$$\nu_T=C_\mu k^2/\varepsilon. \tag{5}$$

C_μ is the coefficient.

The transport equation is more complicated than the *k*–equation, with many unknown second- and third-order moments and many terms that must be simulated using experiments and magnitude analysis.

The typical form of the *k*–equation is as follows:

$$\begin{aligned}\frac{\mathrm{D}\varepsilon}{\mathrm{D}t}&=\frac{1}{\rho}\frac{\partial}{\partial x_k}\left(\frac{\mu_t}{\sigma_e}\frac{\partial\varepsilon}{\partial x_k}\right)+\frac{C_1\mu_t}{\rho}\frac{\varepsilon}{k}\left(\frac{\partial U_l}{\partial x_k}+\frac{\partial U_k}{\partial x_l}\right)\frac{\partial U_l}{\partial x_k}-C_1\frac{\varepsilon^2}{k},\\\frac{\mathrm{D}k}{\mathrm{D}t}&=\frac{1}{\rho}\frac{\partial}{\partial x_k}\left(\frac{\mu_t}{\sigma_k}\frac{\partial k}{\partial x_k}\right)+\frac{\mu_t}{\rho}\left(\frac{\partial U_l}{\partial x_k}+\frac{\partial U_k}{\partial x_l}\right)\frac{\partial U_l}{\partial x_k}-\varepsilon.\end{aligned} \tag{6}$$

Launder and Spalding provide the values of each individual constant:

$$C_\mu=0.09,\ \ C_{\varepsilon1}=1.44,\ \ C_{\varepsilon2}=1.92,\ \ \sigma_e=1.0,\ \ \sigma_\varepsilon=1.3.$$

2.3. Wave Theory

There are many different types of waves in the water, and the dynamic equilibrium between inertial force, gravity, and surface tension defines their physical character. This paper adopts the fifth-order Stokes wave in the numerical pool wave generation because the wave height of a Stokes wave cannot be defined as infinitely small relative to the wavelength, this model can accurately respond to the nonlinear characteristics of shallow water waves, and it is a widely used wave theory in marine engineering calculations.

The potential wave velocity function of Stokes' fifth-order is as follows:

$$\Phi=\frac{c}{k}\sum_{n=1}^{5}\lambda_n\cosh\ nk(z+d)\sin\ n(kx-\omega t). \tag{7}$$

The wavefront equation is

$$\eta = \frac{1}{k}\sum_{n=1}^{5}\lambda_n \cos\ \mathrm{n}(kx-\omega t). \tag{8}$$

The wave speed is

$$kc^2 = C_0^2(1+\lambda^2 C_1+\lambda^4 C_2). \tag{9}$$

The water quality point velocity and acceleration are

$$\begin{aligned} u_x &= \frac{\partial\phi}{\partial x} = c\sum_{n=1}^{5} n\lambda_n \cosh nk(z+d)\cos n(kx-\omega t),\\ u_z &= \frac{\partial\phi}{\partial z} = c\sum_{n=1}^{5} n\lambda_n \sinh nk(z+d)\sin n(kx-\omega t), \end{aligned} \tag{10}$$

$$\begin{aligned} a_x &= \frac{\partial u_x}{\partial t} = \omega c\sum_{n=1}^{5} n^2\lambda_n \cosh nk(z+d)\sin n(kx-\omega t),\\ a_z &= \frac{\partial u_z}{\partial t} = -\omega c\sum_{n=1}^{5} n^2\lambda_n \sinh nk(z+d)\cos n(kx-\omega t). \end{aligned} \tag{11}$$

Once the wave height, period, and water depth are known, it is possible to ascertain the coefficients and wavelengths of the fifth order wave of Stokes by utilizing the dispersion relation.

3. Design and Energy Conversion Mechanism

3.1. China's Offshore Wave Environment

In addition to adhering to the fundamental similarity requirement, the design of the wave energy generator model's parameters should take into account the actual ocean conditions. Figure 1 presents statistical representations of the hydrographic data of the sea region where the wave energy generator is situated in conjunction with earlier studies conducted by academics in China. The Luzon Strait and its western waters account for relatively large values of China's annual average effective wave height, with an annual average wave height of more than 1.8 m, according to the cloud diagram of the annual average effective wave height in China's offshore waters [17]. We referred to the conventional sea trial model and selected a certain scale ratio based on the simulation model. In conclusion, waves in China's offshore waters tend to be between 0.5 and 3 m tall, with periods between 4 and 8 s.

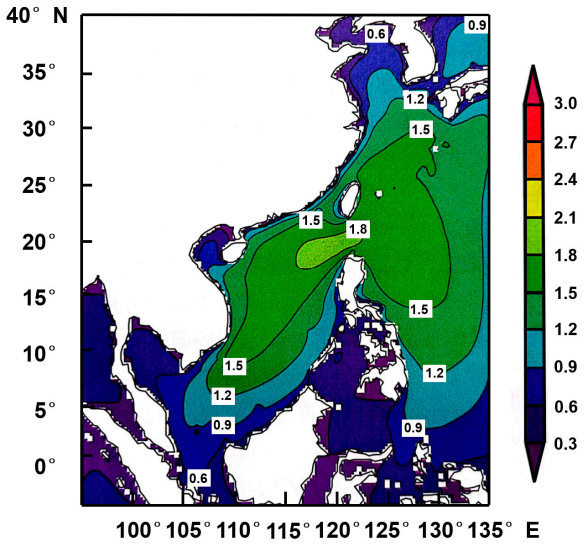

Figure 1. Annual average significant wave height in China's offshore waters (Unit/m).

Therefore, it can be inferred that the simulated wave heights of 0.04 m–0.12 m can fulfill the sea conditions of the real environment [18] when taking into account the probability of the occurrence of wave steepness in the Chinese offshore waters and the CFD numerical simulation circumstances. The wave height of the local wave field will increase sharply and the wavelength will decrease, which poses a significant challenge to the stability and safety of the wave energy generation device when the waves far from the shore propagate to the near shore and are influenced by topography, wind, and current.

In order to better match the more usual wave circumstances in China's actual marine environment, the wave height in this paper was chosen to be between 0.05 and 0.2 m, and the waveform used is the fifth-order Stokes wave.

3.2. Design Proposal

Several factors should be addressed while studying and designing wave energy power production devices, including proper size, the linear damping coefficient, and high mechanical transmission efficiency. A proper overall size can improve the device's application scenario. A suitable linear damping coefficient helps guarantee that wave energy is captured efficiently. The amount of the damping coefficient influences whether waves can readily drive the device. Higher mechanical efficiency can improve the device's energy transmission efficiency.

Because the complicated energy conversion of classic float wave energy power generating devices can result in low power generation efficiency, eliminating intermediate conversion links is critical for boosting device efficiency. Drawing on scientific research, the primary objective of this study is to streamline the composition and elucidate the process of energy conversion in the current oscillating float apparatus, ultimately establishing a novel form of wave energy power generator through oscillating float technology.

Figure 2 displays a three-dimensional depiction of the wave power generator. The Australian-developed "Poseidon" cylindrical float serves as an example of an oscillating float wave power generator. Alan Arthur Wells [19,20], the British engineer specializing in structural engineering, developed the innovative Wells turbine, which operates on low-pressure head air. A detailed representation of the turbine's structure can be observed on the lower left side of Figure 2.

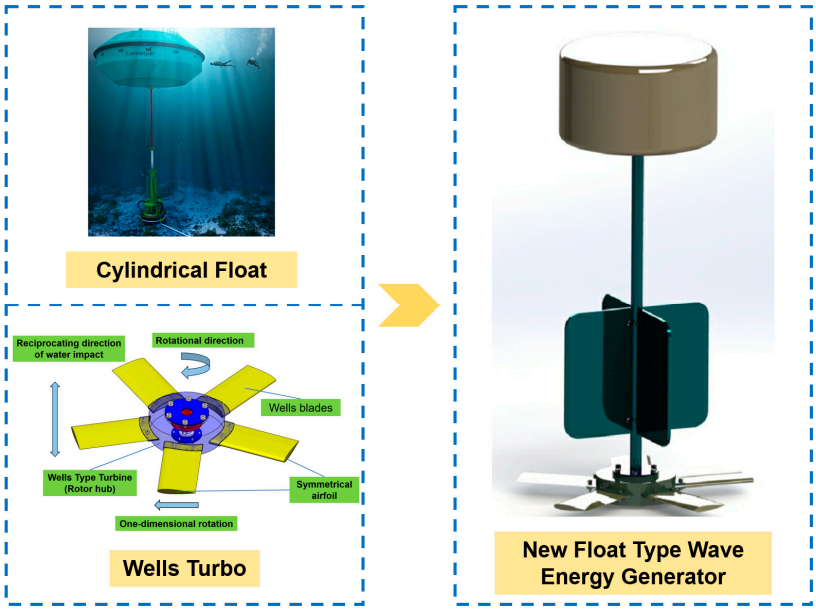

Figure 2. New float-type wave energy generator.

In Figure 2, bottom left, a drawing of the Wells turbine is displayed. The Wells blades are symmetrical airfoils that sustain unidirectional rotation in the reciprocating airflow. It

consists of a symmetrical rotor with numerous sets of airfoil blades positioned along the hub with the chord normal to the rotating axis. It is frequently employed in air turbines for oscillating water column wave energy producers because of its inventive structural construction. It is also the most cost–effective option for wave energy generators due to its simple shape. In this study, a novel float-type wave power generator cleverly integrates the two.

A wave energy producing device must take into account a number of factors, including adequate size, linear damping coefficient, and high mechanical transmission efficiency. According to Figure 3, the design of this device fully incorporates the mechanism of the conventional cylindrical float and the Wells turbine, which can maintain unidirectional rotation under the influence of reciprocating airflow. Through the optimization of the transmission procedure, the device achieves the generation of torque by inducing unidirectional rotation of the blades during the upward and downward motion. This mechanism effectively propels the generator, resulting in power generation at its output.

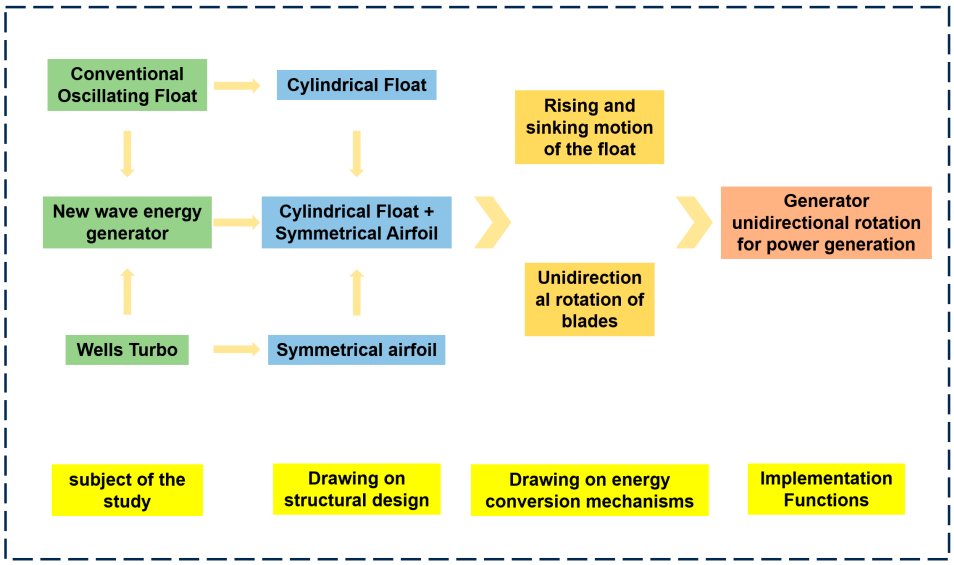

Figure 3. Design ideas for new float-type wave energy generator.

With an overall height of around 600 mm, the novel float-type wave energy generator is seen in Figure 4 below in an exploded view. The float is created in the shape of a hollow and sealed, with a diameter of 200 mm and a height of 120 mm. The overall weight of the device is about 2.8 kg. The float initially floats on the surface of water before moving like a pendulum as a result of the power of the waves. The transmission shaft is attached to the hub and the float through the bearing and the bearing seat, respectively, and the outside edge of the shaft is fitted with a sleeve. It houses a generator and a transmission mechanism.

A sleeve on the shaft's exterior acts as a connector and a protective way of securely connecting the turbofan and the float. The sleeve is fixed with four dampening plates that are 160 mm high but do not participate in the energy transfer. By increasing the efficiency of the device's energy harvesting in the direction of vertical oscillation, the dampening plates' presence can effectively minimize the amplitude of the device's deflection due to pitch and roll.

The novel device's design uses a suspension chain line mooring rope to secure the device's place in the water. Through a gear transmission mechanism, the entire device transfers energy. The power generator for the gadget is a permanent magnet brushless DC generator. The primary element of the energy conversion device and the structural innovation that sets it apart from other wave energy conversion devices is the turbofan

section. As a result, the rotating blade is the primary research object in this paper, and its hydrodynamic properties and operational properties are thoroughly investigated.

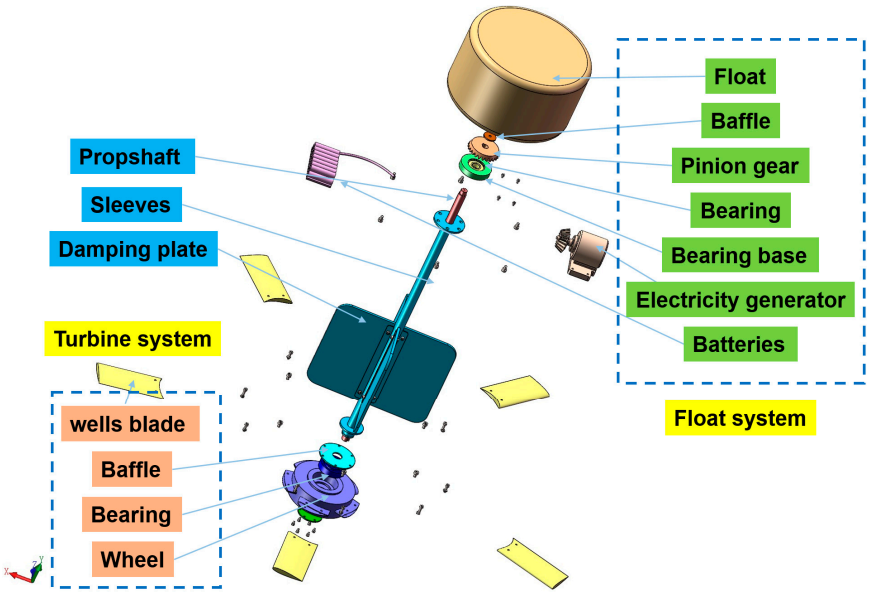

Figure 4. Exploded view of new float-type wave energy generator.

The rectangular bladed NACA0015 symmetric airfoil [21] is used in the turbofan. The blade is 100 mm long, the hub is 100 mm in diameter, and the thickness is 30 mm. The turbofan can successfully rotate unidirectionally in the reciprocating water flow thanks to the symmetric airfoil design. The specifications of the impeller system, which reacts to the float system's action by making a unidirectional rotating motion and driving the generator through the drive shaft to produce power, are shown in Table 1 below.

Table 1. Main parameters of rotating blades.

Parameters	Numerical Value
Number of leaves	5
Chord length/m	0.05
Wheel radius/m	0.05
Flange radius/m	0.05
Wheel thickness/m	0.03

3.3. Characteristics of the Energy Conversion

In a wave energy power generation device, the acquired energy is unidirectionally and irreversibly transferred and converted. The efficiency of energy conversion can be increased by reducing energy loss throughout the transfer process with the aid of a reasonable understanding of the device's energy conversion law. Through its distinctive structural design and transmission mechanism, the new float-type wave energy generator realizes the absorption and conversion of wave energy. Figure 5 depicts the transmission mechanism.

During wave transmission, the float reacts to the wave by oscillating, converting it into linear motion as mechanical energy. It is subjected to the effect of saltwater in the process of pendulum motion and makes a unidirectional rotating motion to transfer mechanical energy because it is rigidly coupled to the turbofan through a sleeve. By means of the drive train, the final generator facilitates the transformation of rotational mechanical energy into electrical energy.

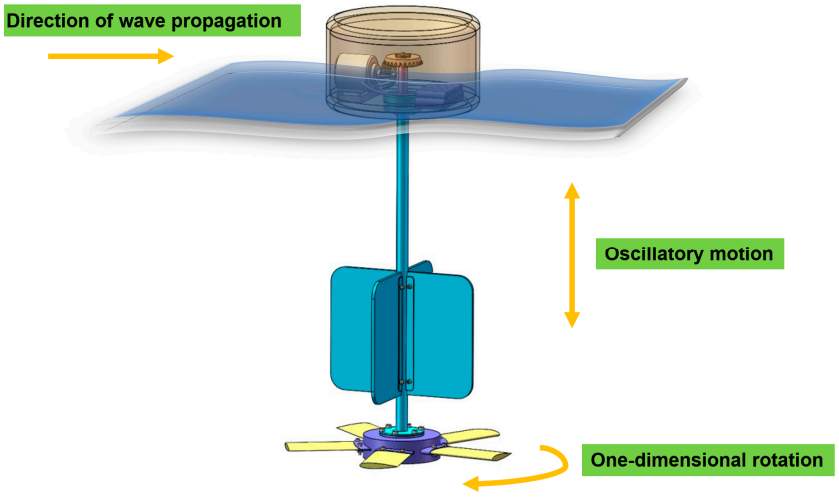

Figure 5. Transmission of the device.

The new wave energy generator, operating as a float-type system, undergoes an energy conversion process. This process is dependent on the efficiency of three components: the float's wave energy capture efficiency η_{cap}, the turbofan's hydrodynamic efficiency η_{hyd}, and the generator's power generation efficiency η_{gen}. The efficiency of the overall wave energy conversion device η can be mathematically represented as follows:

$$\eta = \eta_{cap} \cdot \eta_{hyd} \cdot \eta_{gen}. \tag{12}$$

The three are strongly influenced by nonlinear factors, and the mechanical and electromagnetic relationship is a complex interaction process.

The power input of a vortex fan is typically represented as the kinetic energy of the fluid that flows through the horizontal cross-section of the blades of the fan within a given period.

$$P_{input} = \frac{E_{input}}{t} = \frac{\frac{1}{2}\rho(\pi R^2)hV_A^2}{t} = \frac{1}{2}\rho\pi R^2 V_A^3, \tag{13}$$

At time t, the kinetic energy of a fluid cylinder with height h and radius R traversing the horizontal section of the blade can be represented by E_{input}. V_A denotes the velocity of the fluid relative to the rotating blade's horizontal cross-section.

Output power of turbofan P_{output}:

$$P_{output} = Tw = NT_s w, \tag{14}$$

where T is the output torque of the turbofan, w is the rotational speed (rad/s), N is the number of blades, and T_s is the torque generated by a single blade on the drive shaft.

The brushless DC motor is selected as the generator in the wave energy power generation device in this article. By definition [22], the generator power P is

$$P = \eta \cdot C_l \cdot \dot{x}^2, \tag{15}$$

C_l is the linear damping coefficient, and x is the pendulum displacement of the device.

Generator rotational damping coefficient C_r:

$$C_r = \frac{1.5K_r^2}{R_1 + R_2}, \tag{16}$$

K_r is the torque constant of the generator, R_1 is the generator resistance, and R_2 is the external resistance of the circuit.

C_l can be expressed as

$$C_l = \frac{1.5K_r^2}{\eta(R_1 + R_2)e^2}, \tag{17}$$

The slope, denoted as e, represents the non-linear correlation between the rotational velocity and the velocity at which the device droops. The linear coefficient of damping is associated with the external load and may be regulated to attain the optimal damping ratio and wave capture ratio, which depend on the wave properties, by adjusting the effective value of the external load.

The output power P_{output} of the new float-type wave energy generator involves more variables, and its hydrodynamic characteristics are proposed to be investigated by a combination of theoretical analysis and numerical simulation.

3.4. Kinematic and Dynamic Characterizations

In this paper, the main structural component of energy conversion is the rotating turbofan, so the theoretical analysis focuses on the rotating turbofan part. The rotating blades of the power generation device do not have any change in shape along the direction of the drive shaft and each blade is exactly the same, so the section parallel to the rotating axis and parallel to the airfoil is taken to analyze the motion and force of individual blades. The blade motion and force are shown in Figure 6, and its horizontal cross-section is taken as the reference plane. When seawater impinges on the impeller motion with velocity V_A, it causes a current angle a, which generates a lift force F_L perpendicular to the current direction and a drag force F_D parallel to the current direction.

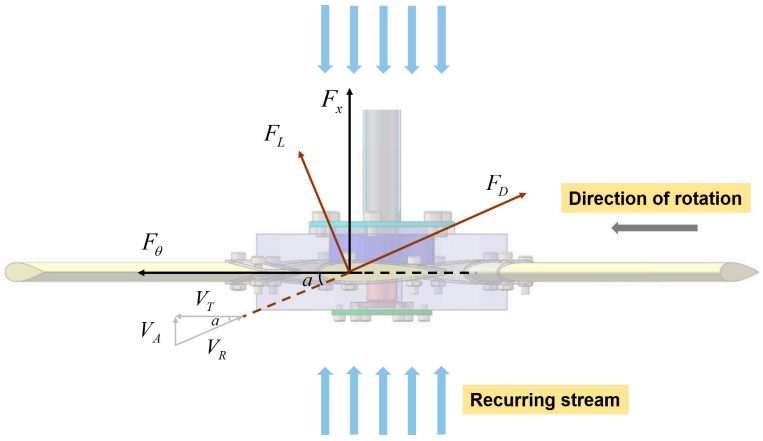

Figure 6. Velocity and force schematic of rotating blade.

As shown in Figure 6, V_T is the circumferential velocity of the fan blades, which is

$$V_T = w \cdot l, \tag{18}$$

where w is the rotational angular velocity of the blade and l is its radial diameter.

Then the combined velocity V_R of the blades relative to the incoming flow is

$$V_R = V_A - V_T. \tag{19}$$

Since V_A and V_T are perpendicular to each other, the mode $|V_R|$ of V_R can be computed in this respect:

$$|V_R| = \sqrt{|V_A|^2 + w^2 l^2}. \tag{20}$$

The water flow angle a is

$$a = \arctan\frac{V_A}{w \cdot l}. \tag{21}$$

The blade lift F_L and drag F_D are

$$F_L = \frac{1}{2}\rho A V_R^2 C_L, \tag{22}$$

$$F_D = \frac{1}{2}\rho A V_R^2 C_D, \tag{23}$$

where ρ is the fluid density, A is the characteristic area of the blade, C_L is the lift coefficient, and C_D is the drag coefficient.

The above forces can be decomposed into an axial force F_x and a tangential force F_θ:

$$F_x = F_L \cos\alpha + F_D \sin\alpha, \tag{24}$$

$$F_\theta = F_L \sin\alpha - F_D \cos\alpha. \tag{25}$$

From the above analysis, it can also be found that for a given value of a, the direction of the tangential force F_θ is independent of the positive or negative value of a. Regardless of the direction of the water flow, the fan blades rotate in one direction.

4. CFD Simulation Analysis of a New Float-Type Wave Energy Device

4.1. Setup of CFD Simulation

In this chapter, a physical model must be chosen in order to calculate the STAR–CCM+. The main goal of the hydrodynamic simulation is to ascertain the dynamic reaction of the novel float-type wave energy generator under various wave circumstances. Table 2 displays the different parameter values used to simulate this paper.

Table 2. Setting of simulation parameters.

Combined Parameters	Physical Models
Space	Three-dimensional
Time	Implicit invariant (math.)
Eulerian multiphase flow model	Volume of fluid domain
Turbulence model	$k-\varepsilon$
Other models	Gravity, VOF waves

The Stokes fifth order waves are used using the boundary condition wave-making approach in this paper. The border satisfies the waves:

Velocity in x direction:

$$u_x = c\sum_{n=1}^{5} n\lambda_n cosh[nk(z+d)] \times cos[n(kx-\omega t)]. \tag{26}$$

Velocity in z direction:

$$u_z = c\sum_{n=1}^{5} n\lambda_n sinh[nk(z+d)] \times sin[n(kx-\omega t)]. \tag{27}$$

The instantaneous rise of the wavefront is

$$\eta = \frac{1}{k}\sum_{n=1}^{5} \lambda_n cos[n(kx-\omega t)], \tag{28}$$

where ω, d, and k are the circular frequency, water depth, and wave number, respectively.

Setting up a wave height meter, as seen in Figure 7, allows for monitoring the time course of the wavefront change on the free surface. It is clear that the waves simulated in this

research are essentially consistent with the theoretical values of the fifth-order Stokes waves, laying the groundwork for an accurate numerical simulation of the subsequent device.

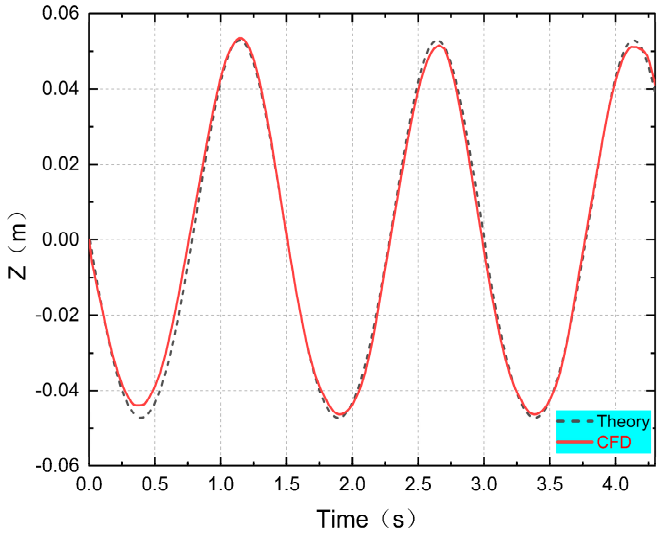

Figure 7. Time history curve of wave height.

To avoid the modification of waveforms and computations in the calculation area caused by wave reflection, the creation of a wave dissipation zone in the outflow region is necessary. This study establishes a length as a damped wave cancellation zone at the pool's outlet end using the damped wave cancellation method [23].

4.2. Computational Domain and Meshing

This article sets up the calculation domain for the fluid simulation computation when the wave period T = 1.5 s, in accordance with the guidelines of the International Towing Tank Conference (ITTC). The distance from the starting point to the boundary where the substance enters is 1λ, while the distance from the starting point to the boundary where the substance leaves is 2λ. The entire extent of the space is 3λ. The depth of the liquid is determined as 1 m, whereas it surpasses the water's surface by 1.08 m. The computational space possesses a width of 2.56 m and a height of 2.08 m. Around 1 million computational grids are secured within the water's surface, background, and the overlapping region of motion [24]. Figure 8 depicts the computational domain case configuration.

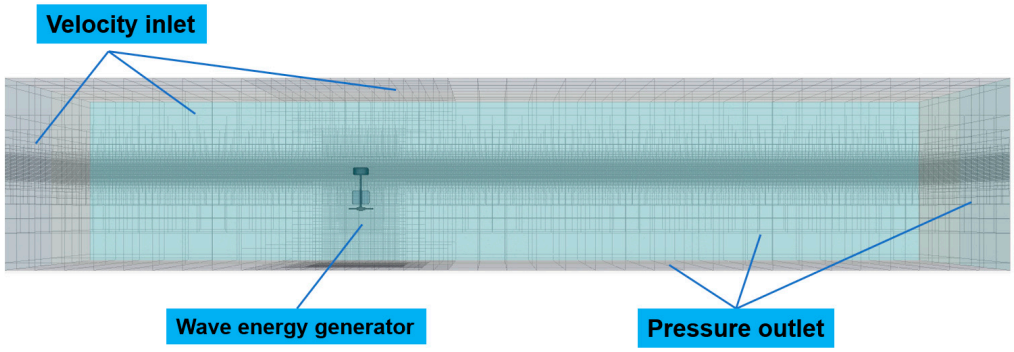

Figure 8. Computational domain setup and meshing.

Overlapping grids are more frequently employed in the CFD simulation of the coupling effect between waves and wave energy producers. The wavefront encrypted area is set up in the backdrop area, and the grid division of the wavefront encrypted area is built up in accordance with the wave parameters' wavelength and wave height H. This

increases computation accuracy and wavefront stability. Figure 9 depicts the situation after encryption. Additionally, the encrypted area is built close to the revolving blade in order to better collect the device's motion state information. The primary encryption approach is to establish surface control and volume control.

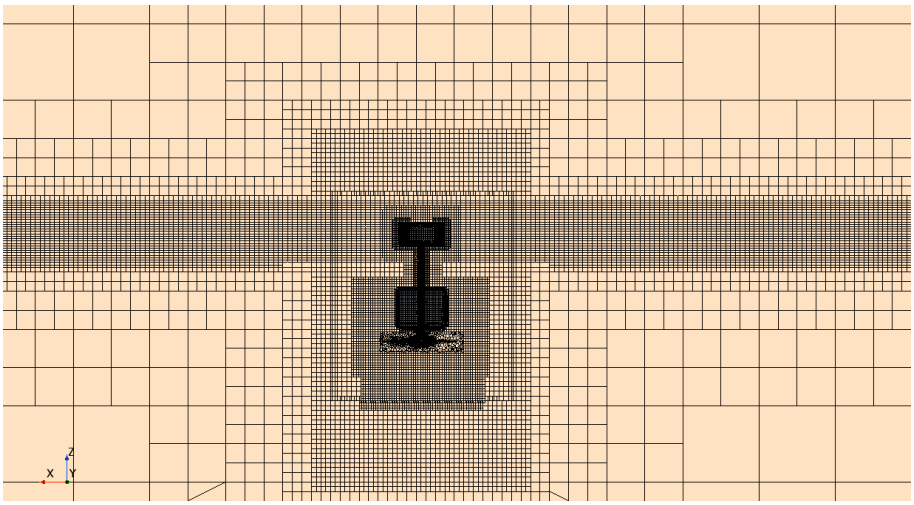

Figure 9. Encryption of meshes.

4.3. Analysis of Device Simulations during One Wave Cycle

The simulation analyzes the movement of the device in the wave with the wave height H = 0.1 m and the period T = 1.5 s in one cycle, and the dynamic simulation interface based on STAR–CCM+ is shown in Figure 10 in order to intuitively understand the law of movement of the power generation device in the wave.

These figures depict the device's status during one operation cycle. Within a cycle, the device goes from the horizontal plane to the peak, then to the trough, then back to the horizontal plane. Because the device's motion is periodic, analyzing the device's motion within one cycle is significant.

The device's overall pendulum motion speed is determined, among other things, by how the floats react to the waves, the inertial forces of the vortex fan, and the fluid resistance. It is clear from Figures 10–12 that the object is moving pendantly. In Figure 10a, orientation is shown as horizontal with minimal vertical displacement. The device is seen moving upwards along the wave surface, reaching its maximum velocity in the positive direction of the Z, measuring 0.151 m/s. Moving on to Figure 10b, the illustration demonstrates the device's upward motion along the wave face, ascending towards the peak of the wave. At this point, the vertical velocity of the pendant oscillation is close to zero at 0.021 m/s, and the greatest displacement is at 0.042 m. The floating body descends down the wave face to the horizontal plane, as shown in Figure 10c, at which point the vertical velocity is close to zero at 0.021 m/s and the displacement of the pendent oscillation achieves its maximum value of 0.042 m. The floating body goes upward along the wave face to meet the wave, as shown in Figure 10c. The device's highest vertical velocity, or 0.146 m/s, is along the Z-axis's negative direction. The floating body has a vertical displacement of 0.042 m. Figure 10e depicts the device making a climbing motion along the wave surface and re–entering at the position of the time plane. Figure 10d depicts the device reaching the trough of the wave, where the vertical displacement of the device in the opposite direction of the extended Z reaches a maximum. The motion of the power generating unit throughout one cycle was described by the comprehensive simulation of Figures 10–12.

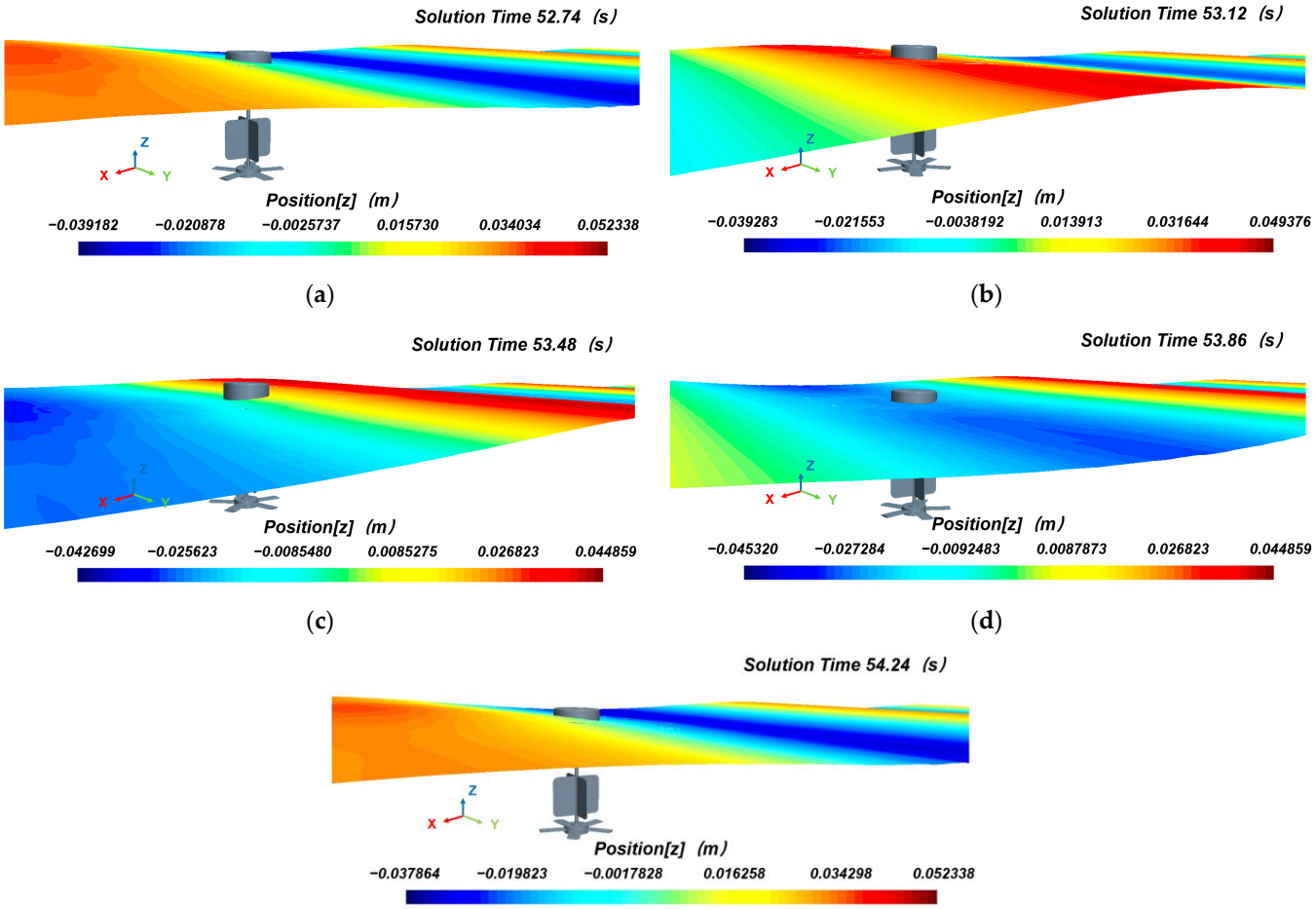

Figure 10. T = 1.5 s, H = 0.1 m diagram of the motion of the power generator in one λ. (**a**) t = 52.74 s; (**b**) t = 53.12 s; (**c**) t = 53.48 s; (**d**) t = 53.86 s; (**e**) t = 54.24 s.

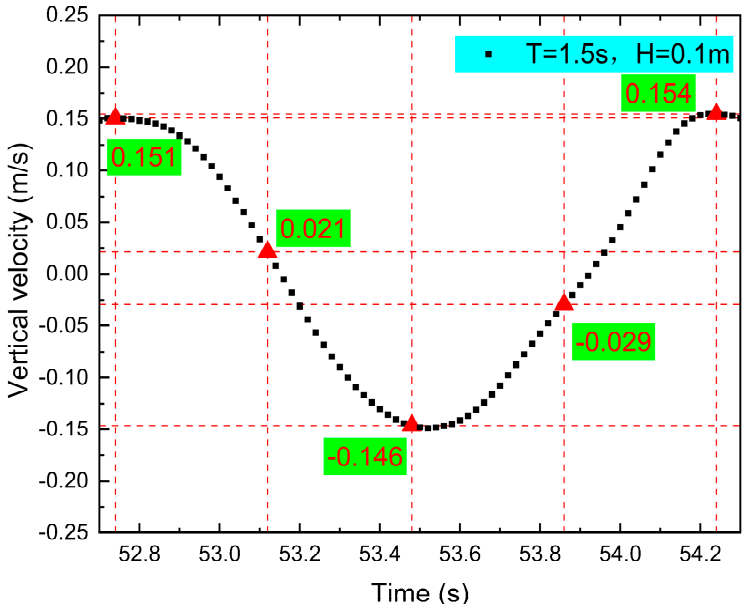

Figure 11. Time history curve of device droop velocity.

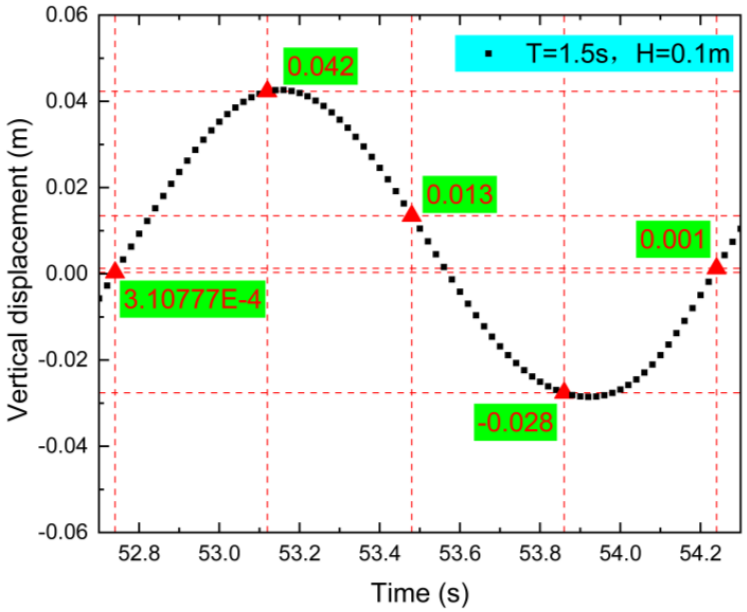

Figure 12. Time history curve of device droop displacement.

The results of the numerical simulation are accurately visualized in Figures 11 and 12 by the use of scatter plots, with a time interval of 0.02 s between each node. Further investigation reveals that the device's movement velocity is decreasing and the velocity decreases more quickly at the point when the device is moving from the horizontal direction towards the crest of the wave, or when the device is moving from 52.74 s to 53.12 s. The device's pendulum velocity in the opposite direction increases slowly and then decreases quickly as it transitions from the peak to the trough, or from 53.12 to 53.86 s. The device's motion velocity in the pendent direction gradually increases as it goes from the wave valley to the horizontal plane, or from 53.86 to 54.24 s, and achieves its maximum at the wave peak. The gadget is subject to both the action of the wave and the action of its own gravity, which results in a certain regularity in the change in speed of motion.

The dynamic pressure cloud of the blades is illustrated in Figure 13. The leading edge of the blade exhibits the highest concentration of pressure, with a maximum pressure difference of 446.18 Pa [25]. The pressure side of the blade is predominantly controlled by positive pressure, while the suction side goes through negative pressure. The output torque of the turbofan is mainly determined by the pressure disparity found at the blade's leading edge [26,27]. Additionally, this analysis acts as an extensive point of reference for a subsequent examination of the device's hydrodynamic efficiency throughout a complete operational cycle.

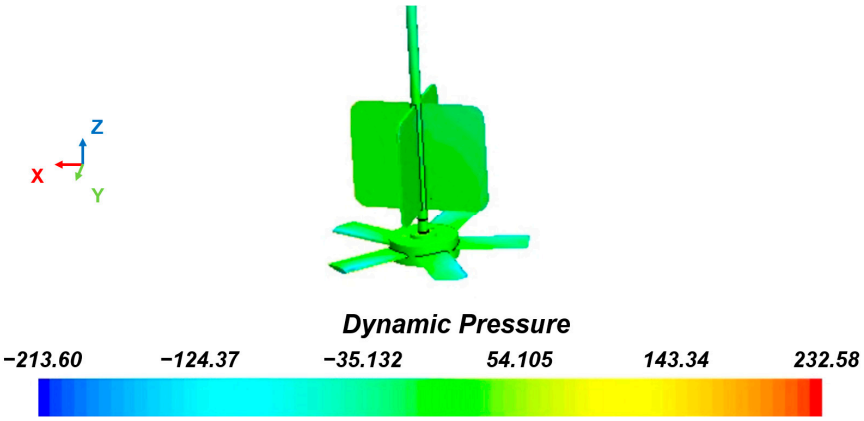

Figure 13. Turbofan dynamic pressure cloud diagram at T = 1.5 s.

A perfect balance between the rotational speed and rotational torque can maximize the power output of the device. The rotational speed of the blades is a significant factor determining the output power and operating parameters of the device. The rotating angular velocity of the blades exhibits regularity, as shown in Figure 14. The turbofan continues to revolve due to inertia at 53.12 s, when the float is at the wave crest position, and at this moment the angular velocity is the least, at roughly 3.419 rad/s.

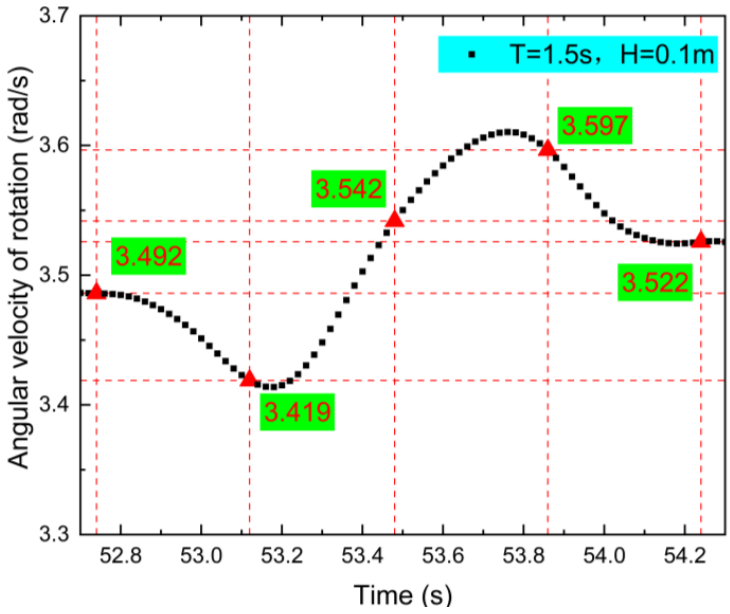

Figure 14. Time history curve of fan blade rotation angular velocity.

The float reaches the wave valley at roughly 53.86 s, and the rotational angular velocity is likewise rapid, at about 3.597 rad/s. The float's angular velocity decreases as it moves from the wave valley to the wave crest, but it considerably increases when it moves from the wave crest to the wave valley position. The angular velocity considerably increases through position.

The turbofan's cycle of instantaneous output power variations is depicted in Figure 15 and is governed by the blade torque and rotational angular velocity. The greatest output power is around 0.05 W during the blade's transition from the crest to the horizontal plane.

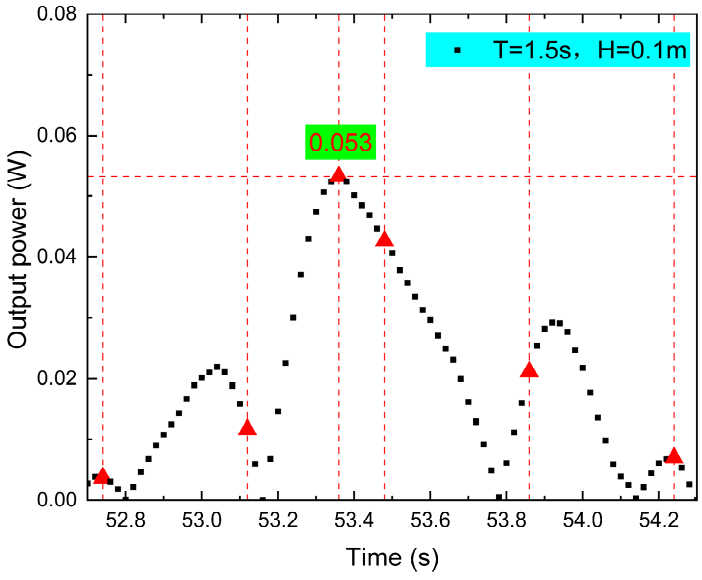

Figure 15. Output power.

The transfer function of the device's motion may be intuitively determined by analyzing how it operates and collects energy in one cycle. Additionally, this analysis acts as an extensive point of reference for a subsequent examination of the device's hydrodynamic efficiency throughout a complete operational cycle.

4.4. Numerical Study of the Effect of Hydrodynamic Performance of Power Generating Units over the Full Operating Cycle

The new float-type wave energy power generating gadget creates periodic motions in the water, and the law may be thought of as the superposition of innumerable periodic motions when the simulation results tend to converge. This part examines the device's force, motion, and power production after it has been operating steadily. Additionally, this portion offers an analytical framework for later optimization of the device's structural properties.

Figures 16 and 17 indicate that after the device has been operating steadily, the pendant velocity and displacement both exhibit periodic fluctuations, with the maximum pendant velocity being around 0.15 m/s. The maximum displacement amplitude of the device, measured in reference to the horizontal plane, is roughly 0.04 m. The device is subjected to buoyancy and gravity during movement, and the unidirectional rotation of the blades can cause disturbance to the water flow, resulting in uneven displacement of the device.

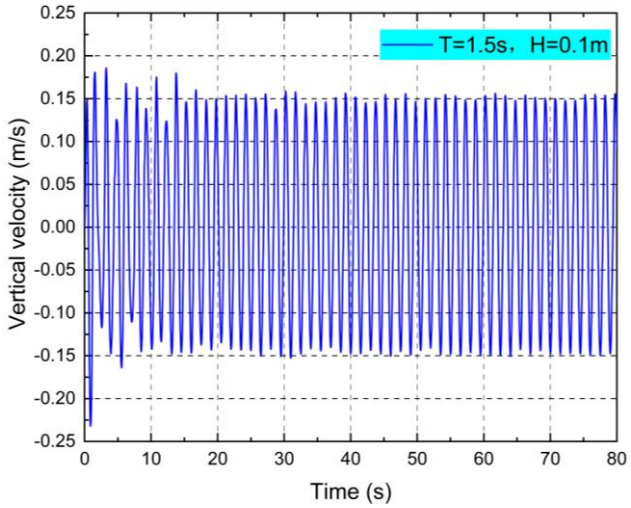

Figure 16. Time–calendar curve of pendulum velocity for full-cycle operation of the device.

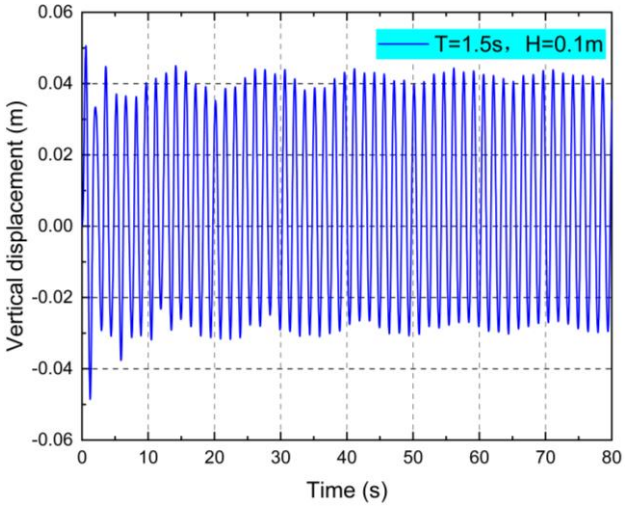

Figure 17. Time–history curves of pendulum displacements for full-cycle operation of the device.

Figure 18 shows that the device's response to the wave moment is periodic, with a larger, approximately 0.015 Nm, blade moment in the valley of the fan blade subjected to reverse rotation and a 0 Nm blade moment in the peak moment. However, due to the turbofan's inertia, the blades continue to rotate even in the case where the blade moment is 0 Nm.

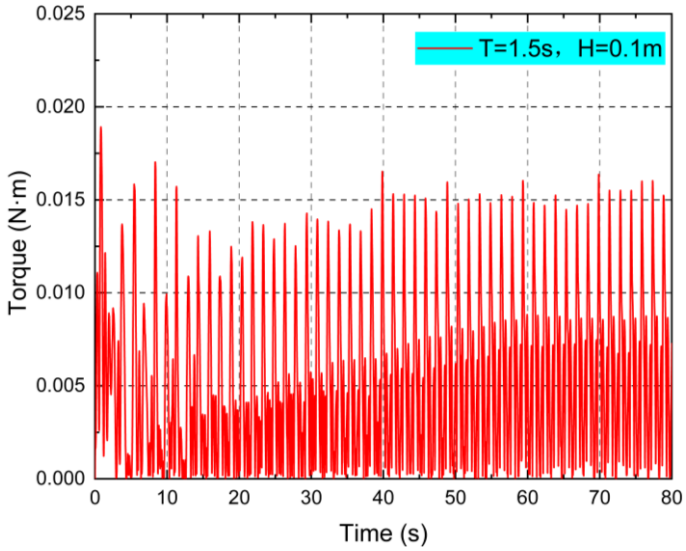

Figure 18. Time–calendar curve of fan blade torque variation for full-cycle operation of the device.

According to Figure 19, the device's rotational angular velocity increases sporadically over time. After 55 s, the blades' rotational angular velocity tends to stabilize at about 3.613 rad/s, which also suggests that at this point the device's motion has reached a converged state.

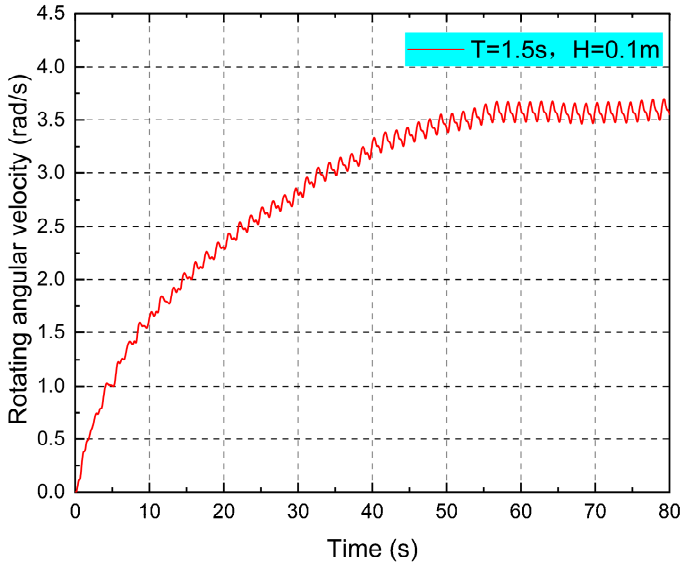

Figure 19. Time–calendar curve of rotational angular velocity variation for full-cycle operation of the device.

The device's output power is influenced by the blade's rotating torque, rotational speed, and transmission efficiency. The output power of the device similarly enters a constant state of change after 55 s and the maximum instantaneous output power is around 0.053 W (as shown in Figure 20).

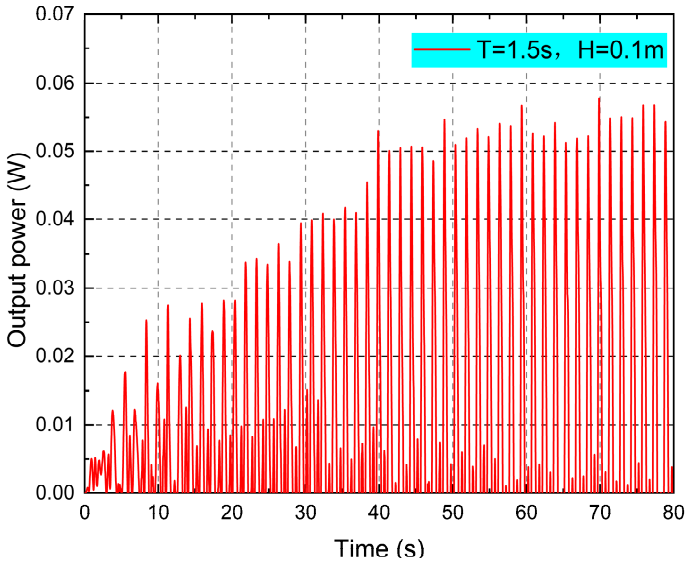

Figure 20. Time–calendar curve of output power change for full-cycle operation of the device.

This part expands from a local analysis to a stable convergence study, concentrating on the hydrodynamic and energy outputs of the device in a single cycle as well as in a whole cycle with a blade number of five. Because changes to the device's structural parameters have no effect on the device's overall general functioning in a wave environment, the research in this part also acts as a comparative reference for the optimization of the structural parameters in the following section.

4.5. Numerical Study of the Effect of Structural Parameters on the Hydrodynamic Performance of Power Generation Units

One of the crucial factors in the structural design of a rotating turbofan is the number of its blades; too many or too few moving elements on the impeller will influence the device's dependability and performance qualities. This section analyzes the bottom rotating turbofan force and motion response in waves using four different devices with three, four, five, and six blades. Table 3 displays the chosen operating conditions.

Table 3. Main parameters for different number of blades.

Working Condition	Number of Leaves	Period T(s)	Wave Height (m)
A_1	3	1.5	0.1
A_2	4	1.5	0.1
A_3	5	1.5	0.1
A_4	6	1.5	0.1

The analysis of the device's motion in the wave primarily utilizes major factors including the velocity of motion along the direction of the overall pendulum oscillation, displacement, moment exerted by the blade, rotational speed of the vortex fan, dynamic pressure, and power generated as output [28]. The device's oscillatory displacement and velocity exhibit periodic changes, as shown in Figures 21 and 22. The number of blades has less of an impact on the pendulum displacement and pendulum velocity of the device.

The time–domain curve of the moment of the turbofan blades is depicted in Figure 23. The rotational moment is significantly impacted by the periodic fluctuations in the blade moment caused by the action of the waves. When there are six blades, the rotational torque is greatest when compared with other circumstances. The greatest moment amplitude is around 0.012 Nm, whereas the smallest moment amplitude is about 0.008 Nm. With an increase in blade count, the spinning moment of the blades increases.

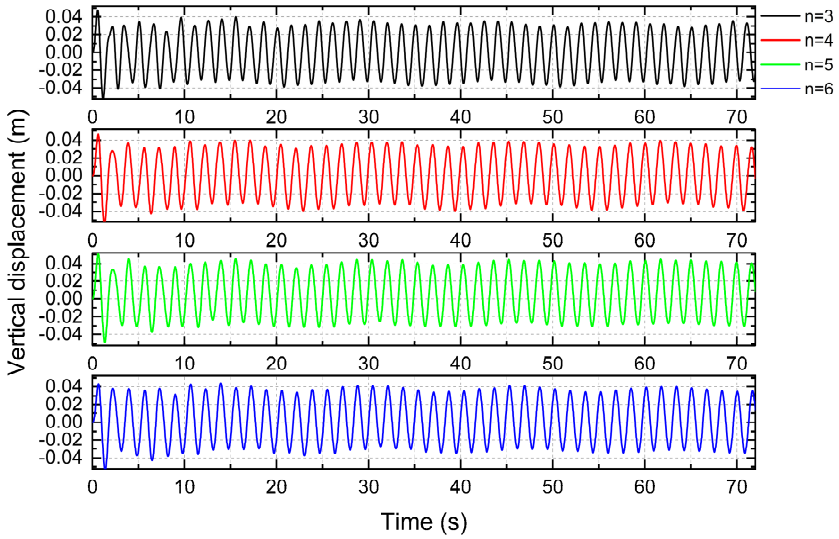

Figure 21. Encrypt vertical displacement.

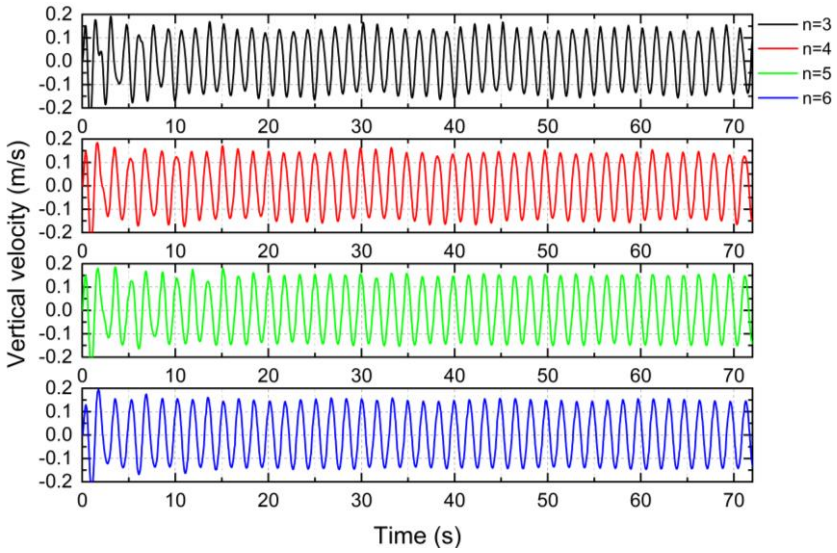

Figure 22. Vertical velocity.

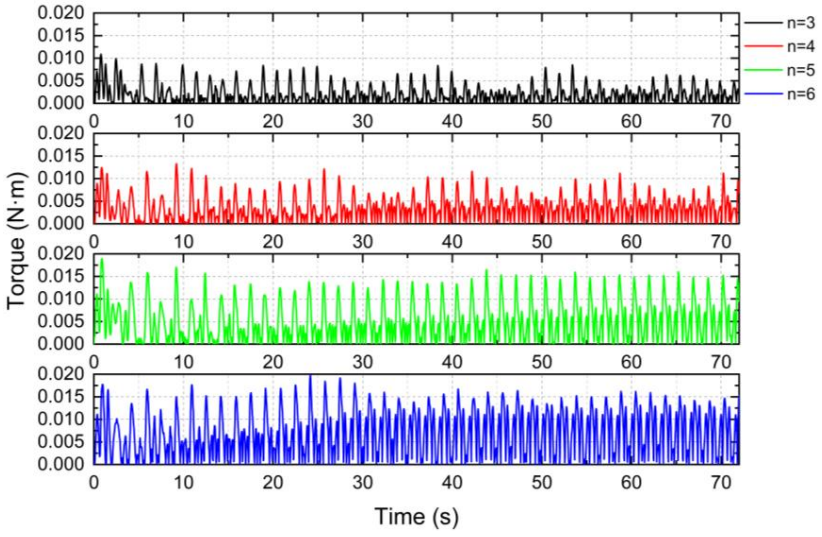

Figure 23. Time history curve of fan blade torque.

The time–calendar curve of the turbofan's angular velocity is depicted in Figure 24. As seen in the image, the turbofan's rotating angular velocity steadily rises with the number of blades and, over time, tends to stabilize for all of them. The convergence of the turbofan rotational speed is very similar when there are five and six blades. The rotational speed of a turbofan with five blades is approximately 3.613 rad/s and a turbofan with six blades is approximately 3.707 rad/s, which is somewhat higher than the constant rotational speed of these two devices. The turbofan speed converges steadily to 2.11 rad/s, the minimum speed, when there are three blades. As can be seen, the turbofan speed increases steadily as the number of blades grows and will eventually converge to a steady value.

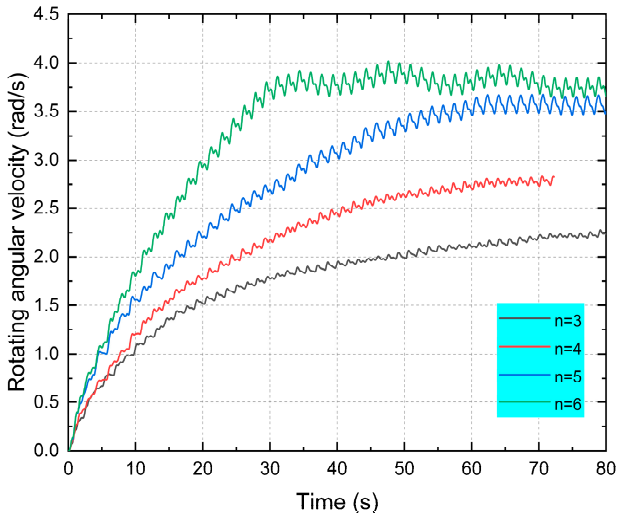

Figure 24. Time history curve of blade rotation speed.

The comparative analysis of Figures 13 and 25 unveils the similarities in the cloud diagrams illustrating the dynamic pressure of the four distinct device types. It becomes evident that the distribution pattern of blade pressure exhibits resemblances. Specifically, the leading edge predominantly houses the high-pressure region, while the differential pressure on the blade surface gradually diminishes along the chord length, eventually approaching zero near the trailing edge section [29].

When there are three blades, the maximum differential pressure of the blade is 139.556 Pa; when there are four blades, the maximum differential pressure is 338.257 Pa; and when there are six blades, the highest differential pressure is 424.52 Pa.

With an increase in the number of blades, the differential pressure at the leading edge of the blade surface gradually rises. In other words, a sufficient increase in the number of blades can increase the pressure differential between the two sides of the leading edge of the blades, increase the size of the high-pressure differential zone, and consequently enable the turbofan to produce a greater rotating torque. This study also found that increasing the velocity relative to the blade's leading edge can enhance the pressure disparity on both sides. This expansion of the high-pressure difference region leads to a greater rotational torque within the absorber. The blade pressure is negative, and the blade can spin in one direction as long as the pressure differential on both sides of the blade is bigger than the back chord.

Figure 26 displays a graph of the device's instantaneous output power. It is evident that, after some time in the same wave environment, the output power of the power production equipment tends towards a stable amplitude of change. The turbofan's highest instantaneous output power is 0.059 W when it has six blades, while its lowest instantaneous output power is approximately 0.012 W when it has three blades. It was discovered that the instantaneous output power rises with the number of blades when the other three conditions are combined.

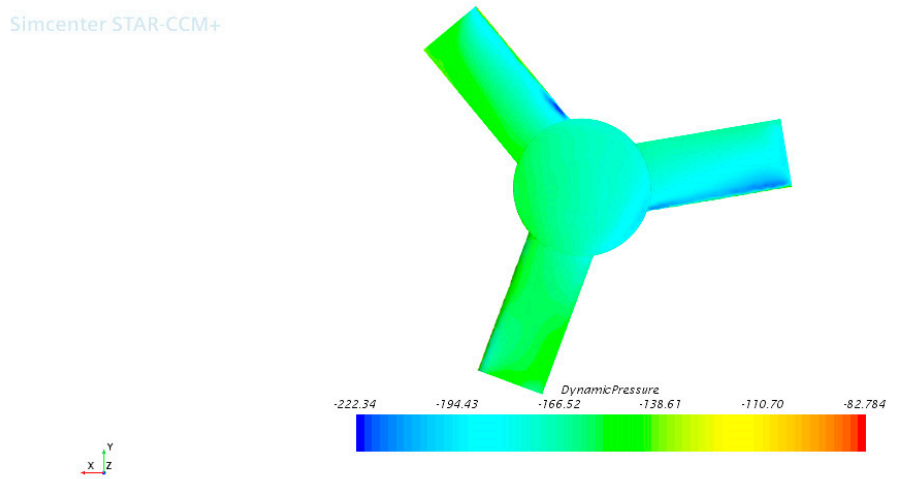

(**a**)

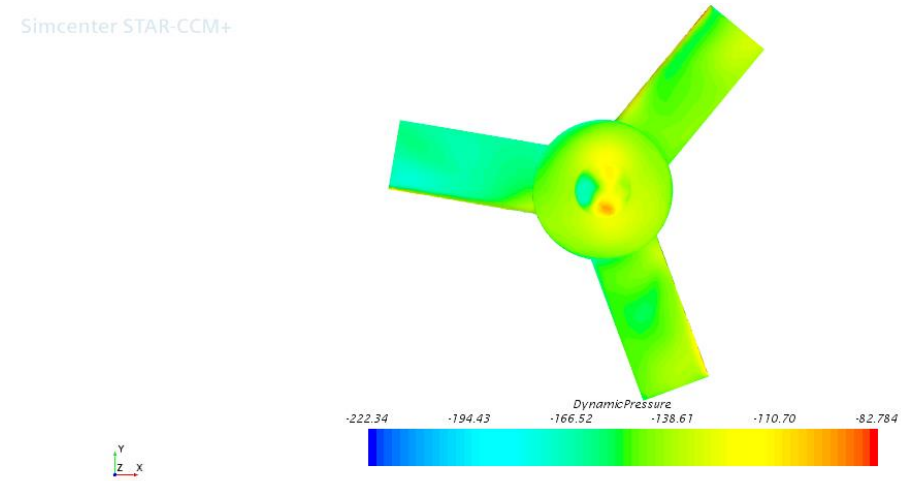

(b)

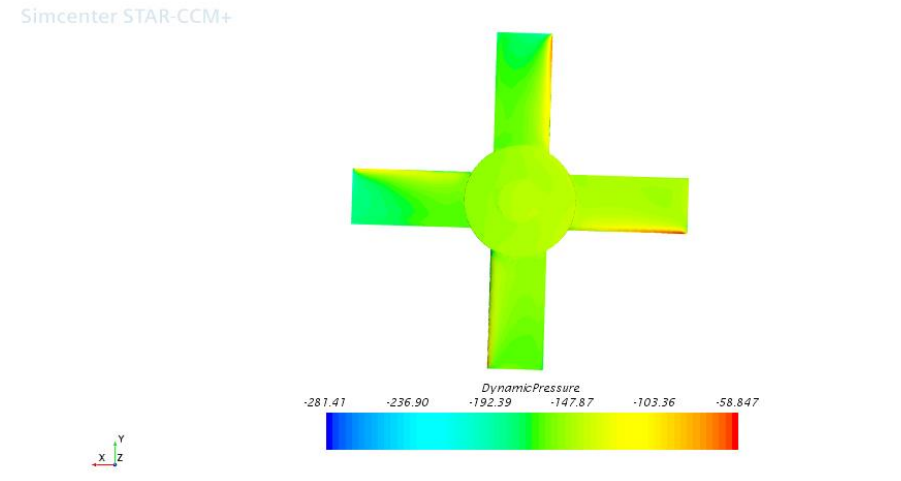

(c)

Figure 25. *Cont*.

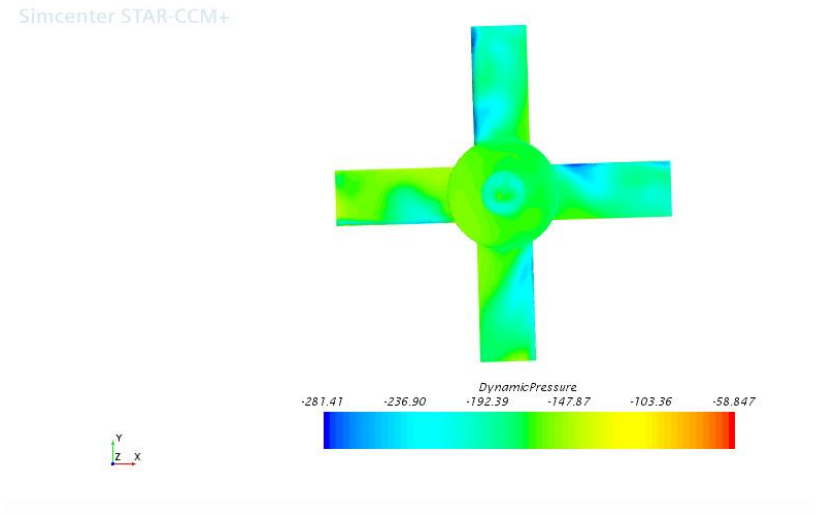

(d)

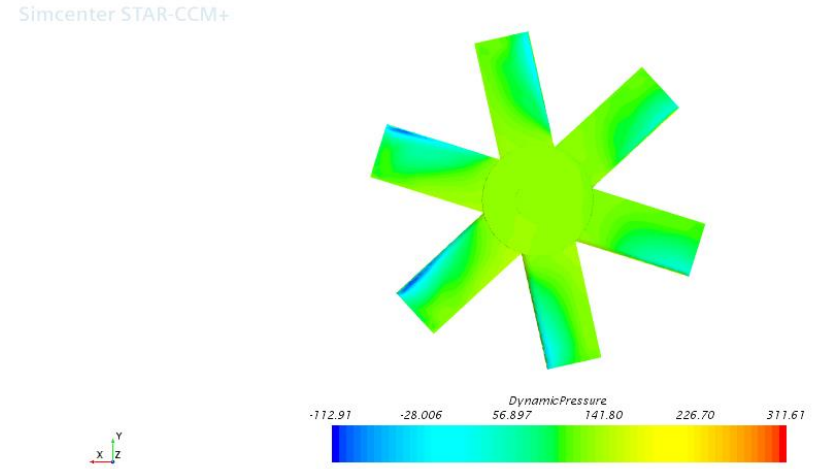

(e)

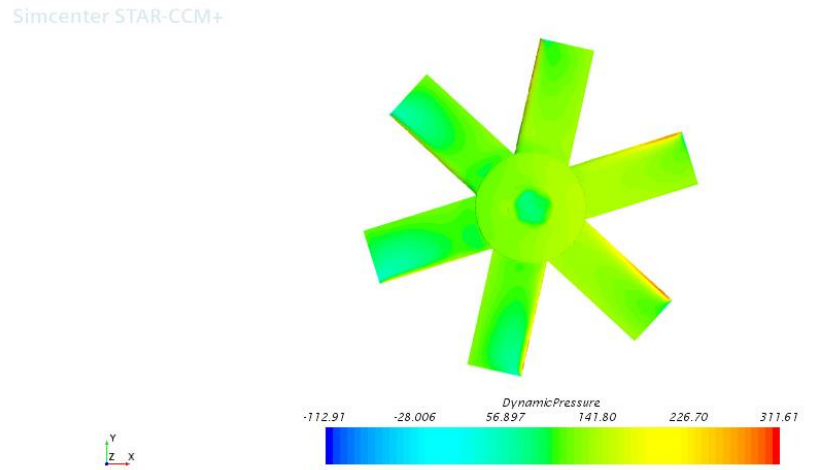

(f)

Figure 25. Turbofan dynamic pressure clouds for devices with different blade numbers. (**a**) Pressure side of turbofan with three-bladed unit; (**b**) Suction side of turbofan with three-bladed unit; (**c**) Pressure side of turbofan with four-bladed unit; (**d**) Suction side of turbofan with four-bladed unit; (**e**) Pressure side of turbofan with six-bladed unit; (**f**) Suction side of turbofan with six-bladed unit.

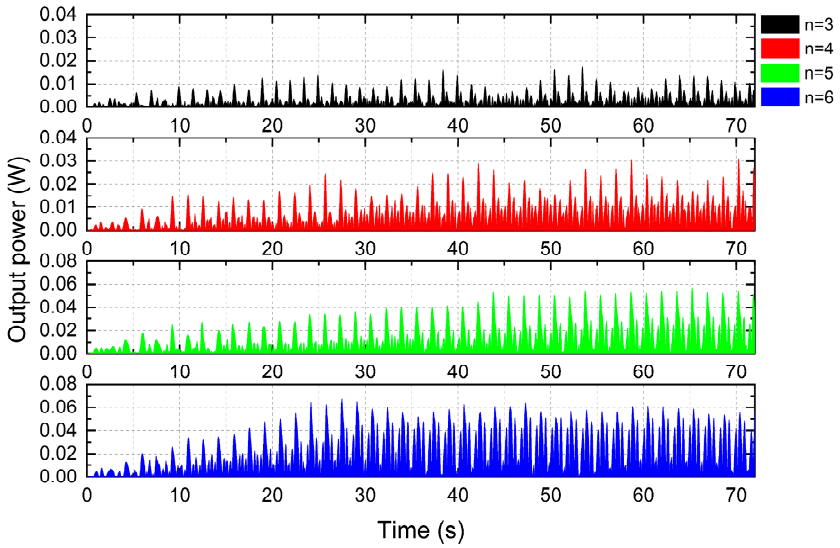

Figure 26. Output power of units with different blades.

Table 4 summarizes the findings of the calculations made by adding up all the calculated working conditions:

Table 4. Comparison of calculation results.

Working Condition	Amplitude of Pendulum Displacement (m)	Amplitude of Pendulum Speed (m/s)	Amplitude of Rotational Torque (N·m)	Rotational Speed (rad/s)	Power (W)
A_1	0.372	0.158	0.004	2.352	0.012
A_2	0.381	0.157	0.009	2.831	0.023
A_3	0.407	0.161	0.014	3.613	0.053
A_4	0.411	0.159	0.015	3.707	0.059

As shown in Table 4, when there are five blades, the device's pendulum oscillation speed is higher, averaging 0.161 milliseconds, and the instantaneous output power is comparatively high at this time, second only to the six-bladed device. The number of blades has less of an impact on the generator's overall pitching displacement and pitching speed [30].

As the number of blades increases, the turbofan's rotational speed gradually rises, as does the rotational torque, which is caused by an increase in the ratio of the high-pressure differential area to the area of a single blade. In terms of rotation speed, as the number of blades grows, the device's power and rotation speed steadily increase. We also referred to the option of floating fans for the setting of the five blades for the five and six blades. At the moment, cost is a major impediment to the development of innovative energy gadgets. On the one hand, we examined the structure's rotating speed and output power. Based on this, we believe that fewer blades are preferable. In other ways, it is to cut costs. As a result, the device's overall torque rises, as does the power output, and the five-bladed turbofan's overall performance is better from the standpoint of efficiency.

5. Conclusions

This paper presents a novel float-type wave energy power generation device specifically designed for the offshore wave environment in Asia. The objective of this study is to develop a wave energy power generation device that incorporates a simple transmission method, allows for flexible layout, and achieves high conversion efficiency. The study begins by analyzing the operational behavior of the device within a single cycle under optimal wave conditions (simulation period: 1.5 s, wave height: 0.1 m). Subsequently, the

hydrodynamic performance of the crucial impeller system is examined, with a particular focus on the impact of varying blade numbers on device performance, in order to identify the optimal design solution. The following specific conclusions are drawn:

1. We constructed a numerical wave pool using STAR-CCM+ and applied overlapping grid technology to simulate the movement and power generation efficiency of a new float-type wave energy power generation device under Stokes fifth-order waves. Our findings indicate that this numerical method accurately captures changes in complex flow fields, and the simulated waves closely match the theoretical waves. Hence, it can serve as a reliable tool for numerical simulation of this device.
2. In operation following the stability of the law, the new type of float wave power generating device in saltwater to perform the cycle movement may be viewed as the superposition of the movement of countless cycles. The device's speed drops as it moves from the horizontal to the crest of the movement of the moment, and the speed declines ever faster, according to the examination of the device's movement in a cycle. The pendulum velocity of the device increases slowly and then lowers quickly as it transitions from the crest to the trough. The device's motion speed in the vertical direction gradually increases until it reaches its maximum speed at the wave peak as it passes from the wave valley to the horizontal plane. The torque and speed of the rotating blades have a significant impact on the device's output power.
3. According to the structural design and optimization of the device, it was found that the overall movement of the device is less affected by changes in the number of blades, and regardless of the changes in the number of blades, the vertical displacement and velocity of the device exhibit periodic changes. Under the influence of waves, the moment of the blades varies on a regular basis, and the moment of the blades rises as the number of blades grows. A suitable increase in the number of blades can cause the turbofan to create a greater rotating moment because the pressure differential at the leading edge of the blade surface steadily increases with the number of blades. The output power of the device increases with the number of blades, and the five blades turbofan performs better overall in terms of equipment cost, operation, and power generation efficiency.

Author Contributions: Writing—original draft, Y.Z.; Writing—review & editing, D.L. All authors have read and agreed to the published version of the manuscript.

Funding: This research received no external funding.

Data Availability Statement: Data are contained within the article.

Acknowledgments: We appreciate the journal's editors and reviewers for their insightful criticism of the research.

Conflicts of Interest: The authors declare no conflict of interest.

References

1. Side, J.; Gallego, A.; James, M.; Davies, I.; Heath, M.; Karunarathna, H.; Venugopal, V.; Vögler, A.; Burrows, M. Developing methodologies for large scale wave and tidal stream marine renewable energy extraction and its environmental impact: An overview of the Tera Watt project. *Ocean Coast. Manag.* **2017**, *147*, 1–5. [CrossRef]
2. Leeney, R.H.; Greaves, D.; Conley, D.; O'Hagan, A.M. Environmental Impact Assessments for wave energy developments—Learning from existing activities and informing future research priorities. *Ocean Coast. Manag.* **2014**, *99*, 14–22. [CrossRef]
3. Venugopal, V.; Nemalidinne, R.; Vögler, A. Numerical modelling of wave energy resources and assessment of wave energy extraction by large scale wave farms. *Ocean Coast. Manag.* **2017**, *147*, 374–378. [CrossRef]
4. Wang, X.; Liang, H.; Qiao, D.; Yan, J.; Ning, D.; Ou, J. Hardware-In-the-Loop test for the optimal damping identification of oscillating buoy wave energy converters. *Ocean Eng.* **2023**, *287*, 115730. [CrossRef]
5. Salter, S.H. Wave power. *Nature* **1974**, *249*, 720–724. [CrossRef]
6. Korde, U.A. Phase control of floating bodies from an on-board reference. *Appl. Ocean Res.* **2001**, *23*, 2512–2562. [CrossRef]
7. Eriksson, M.; Isberg, J.; Leijon, M. Hydrodynamic modelling of a direct drive wave energy converter. *Int. J. Eng. Sci.* **2005**, *43*, 1377–1387. [CrossRef]

8. Babarit, A.; Clément, A.H. Optimal latching control of a wave energy device in regular and irregular waves. *Appl. Ocean Res.* **2006**, *28*, 77–91. [CrossRef]
9. De Backer, G.; Vantorre, M.; Frigaard, P.; Beels, C.; De Rouck, J. Bottom slamming on heaving point absorber wave energy devices. *J. Mar. Sci. Technol.* **2010**, *15*, 119–130. [CrossRef]
10. Negri, M.; Malavasi, S. Wave Energy Harnessing in Shallow Water through Oscillating Bodies. *Energies* **2018**, *11*, 2730. [CrossRef]
11. Marchesi, E.; Negri, M.; Malavasi, S. Development and analysis of a numerical model for a two-oscillating-body wave energy converter in shallow water. *Ocean Eng.* **2020**, *214*, 107765. [CrossRef]
12. Zhang, H.; Zhou, B.; Vogel, C.; Willden, R.; Zang, J.; Geng, J. Hydrodynamic performance of a dual-floater hybrid system combining a floating breakwater and an oscillating-buoy type wave energy converter. *Appl. Energy* **2020**, *259*, 114212. [CrossRef]
13. Curto, D.; Franzitta, V.; Guercio, A. Sea Wave Energy. A Review of the Current Technologies and Perspectives. *Energies* **2021**, *14*, 6604. [CrossRef]
14. Khan, M.Z.A.; Khan, H.A.; Aziz, M. Harvesting Energy from Ocean: Technologies and Perspectives. *Energies* **2022**, *15*, 3456. [CrossRef]
15. Ahn, S.; Haas, K.A.; Neary, V.S. Wave energy resource characterization and assessment for coastal waters of the United States. *Appl. Energy* **2020**, *267*, 114922. [CrossRef]
16. Plummer, M.L.; Feist, B.E. Capturing energy from the motion of the ocean in a crowded sea. *Coast. Manag.* **2016**, *44*, 4644–4685. [CrossRef]
17. Zheng, C. Theoretical Research on the Utilization of Renewable Energy (Wave Energy, Wind Energy) Resources at Sea. Ph.D. Thesis, National University of Defense Technology, Changsha, China, 2020.
18. Chen, W.; Dolguntseva, I.; Savin, A.; Zhang, Y.; Li, W.; Svensson, O.; Leijon, M. Numerical modelling of a point-absorbing wave energy converter in irregular and extreme waves. *Appl. Ocean Res.* **2017**, *63*, 901–905. [CrossRef]
19. Wang, X.S.; Wang, L.H.; Song, X.F.; Ning, B. 3D Wave Simulation Basing on VOF Method and Dynamic Grid Technology. *Adv. Mater. Res.* **2013**, *774*, 3443–3446. [CrossRef]
20. Kotb, A.T.M.; Nawar, M.A.A.; Abd El Maksoud, R.M.; Mohamed, M.H. Comprehensive and synergistic analysis of geometry effect on an axial turbine performance for wave energy conversion. *Ocean Eng.* **2021**, *233*, 109212. [CrossRef]
21. Noel, A.B.; Abdaoui, A.; Elfouly, T.; Ahmed, M.H.; Badawy, A.; Shehata, M.S. Structural health monitoring using wireless sensor networks: A comprehensive survey. *IEEE Commun. Surv. Tutor.* **2017**, *19*, 1403–1423. [CrossRef]
22. Cambuli, F.; Ghisu, T.; Virdis, I.; Puddu, P. Dynamic interaction between OWC system and Wells turbine: A comparison between CFD and lumped parameter model approaches. *Ocean Eng.* **2019**, *191*, 106459. [CrossRef]
23. Setoguchi, T.; Takao, M. Current status of self rectifying air turbines for wave energy conversion. *Energy Convers. Manag.* **2006**, *47*, 2382–2396. [CrossRef]
24. Zhang, Y.; Wu, P.; Duan, M. A mesh-independent technique to evaluate stress singularities in adhesive joints. *Int. J. Adhes. Adhes.* **2015**, *57*, 105–117. [CrossRef]
25. Zhang, Y.; Li, D.Q.; Hong, S.H.; Zhang, M. Design of a new oscillating-buoy type wave energy converter and numerical study on its hydrodynamic performance. *Hrčak* **2023**, *74*, 145–168. [CrossRef]
26. Falnes, J. Wave-energy conversion through relative motion between two single-mode oscillating bodies. *J. Offshore Mech. Arct. Eng.* **1999**, *121*, 32–38. [CrossRef]
27. Zhang, Y.; Duan, M.; Wang, Y.; Chu, G. Analytical study of the strength of adhesive joints of riser pipes. *Ships Offshore Struct.* **2015**, *10*, 545–553. [CrossRef]
28. Cui, Y.; Hyun, B.-S. Numerical study on Wells turbine with penetrating blade tip treatments for wave energy conversion. *Int. J. Nav. Archit. Ocean Eng.* **2016**, *8*, 4564–4565. [CrossRef]
29. Zhao, X.; Xue, F.; Chen, L.; Göteman, M.; Han, D.; Geng, J.; Sun, S. Hydrodynamic analysis of a floating platform coupled with an array of oscillating bodies. *Ocean Eng.* **2023**, *287*, 115439. [CrossRef]
30. Cui, Y.; Zhao, H. Marine renewable energy project: The environmental implication and sustainable technology. *Ocean Coast. Manag.* **2022**, *232*, 106415. [CrossRef]